Polymer Testing 114 (2022) 107717

Contents lists available at ScienceDirect

Polymer Testing

journal homepage: www.elsevier.com/locate/polytest

Impact of stress triaxiality, strain rate, and temperature on the mechanical response and morphology of PVDF

Jonas Hund [a,*], Henrik Møgster Granum [b], Sindre Nordmark Olufsen [a], Petter Henrik Holmström [c], Joakim Johnsen [a,b], Arild Holm Clausen [a]

[a] Department of Structural Engineering, NTNU, Richard Birkelands vei 1A, 7491, Trondheim, Norway
[b] Enodo AS, Richard Birkelands vei 1A, 7034, Trondheim, Norway
[c] Equinor ASA, Arkitekt Ebbells veg 10, 7053, Ranheim, Norway

ARTICLE INFO

Keywords:
Semi-crystalline polymer
Material characterisation
Poly-vinylidene fluoride
Viscoplasticity
Pressure-sensitive yielding
Void growth

ABSTRACT

Poly-vinylidene fluoride (PVDF) is a semi-crystalline thermoplastic featuring a high chemical resistance, good thermal stability, and high pressure resistance, rendering it attractive for a wide range of engineering applications. This study assesses the influence of temperature, strain rate, and stress triaxiality on the large-strain response of a commercial PVDF copolymer containing poly-ethylene (PE) particles.

The thermo-viscoplastic response of the material was investigated at six temperatures ranging between −20 °C and 100 °C at a quasi-static strain rate $\dot{e}$ of 0.005 s^{-1}, and three strain rates $\dot{e} = \{0.005, 0.1, 1.0\}$ s^{-1} at room temperature. To study the pressure sensitivity of the material, tensile tests using axisymmetric notched tensile specimens with three different notch radii as well as uniaxial compression tests were performed. The mechanical response was assessed in terms of net axial stress and volume strain *vs.* longitudinal strain, measured using digital image correlation (DIC). To gain insight into the interrelationship between the macroscopic volume strain and void morphology on the microscale, selected cross sections of deformed specimens were imaged employing scanning electron microscopy (SEM).

The material exhibited a temperature- and strain-rate-dependent response as well as a pressure-sensitive flow stress. For ambient temperatures up to 60 °C, pronounced plastic dilatancy was observed, promoted by increasing the stress triaxiality. The SEM study confirmed that the plastic dilatancy was a result of extensive void nucleation and growth on the microscale. Two sources of void nucleation were identified, namely particle–matrix interface separation as well as cavitation within the matrix material itself. In tests performed at ambient temperatures higher than 80 °C, no plastic dilation was observed and no voids or PE particles were identified in the SEM images.

Apart from an improved understanding of the material's mechanical response, this study provides data and insights suitable for the development and calibration of constitutive models, aiding the design of robust and reliable structures using PVDF.

1. Introduction

Poly-vinylidene fluoride (PVDF) is a semi-crystalline thermoplastic polymer with high chemical resistance, good thermal stability, and high pressure resistance [1–3]. In addition, PVDF has favourable piezo-electrical properties associated with a transformation of its common apolar α crystalline phase into the polar β crystalline phase [4–8]. Thus, PVDF has become a popular engineering polymer used in a wide range of applications such as microfiltration membranes [9], pressure sensors [10], and pressure barriers in the oil and gas industry [11].

To design robust, material-efficient, and sustainable structures, detailed knowledge of the material's large-strain response under the relevant loading conditions is essential. However, despite the widespread use of PVDF, the availability of experimental data suitable for modelling the large-strain mechanical response of PVDF at different loading conditions and temperatures is limited.

* Corresponding author.
E-mail addresses: jonas.hund@ntnu.no (J. Hund), henrik@enodo.no (H.M. Granum), sindre.n.olufsen@ntnu.no (S.N. Olufsen), joakim.johnsen@ntnu.no (J. Johnsen), arild.clausen@ntnu.no (A.H. Clausen).
URLs: https://www.ntnu.no/ansatte/jonas.hund (J. Hund), https://www.enodo.no/ (H.M. Granum), https://www.ntnu.no/ansatte/sindre.n.olufsen (S.N. Olufsen), https://www.ntnu.no/ansatte/joakim.johnsen (J. Johnsen), https://www.ntnu.no/ansatte/arild.clausen (A.H. Clausen).

https://doi.org/10.1016/j.polymertesting.2022.107717
Received 28 April 2022; Received in revised form 24 June 2022; Accepted 19 July 2022
Available online 23 July 2022

As is common for thermoplastic polymers, PVDF exhibits a thermo-viscoelastic and thermo-viscoplastic response where the yield stress and elastic modulus increase for increasing strain rate and decreasing temperature [12]. Another characteristic of PVDF is the occurrence of stress-whitening during deformation, associated with an increased degree of crystallinity [1,12,13] as well as nucleation and growth of voids within the material [3,12].

Void nucleation and growth is a common observation in thermoplastics, corresponding to pressure-sensitive yielding as well as plastic dilation [14,15]. Void nucleation in un-filled PVDF can be observed even prior to yielding, caused by the formation of nanometer to micrometer sized cavities within the amorphous inter-laminar phase of the microstructure [16]. This behaviour is a common observation in semi-crystalline polymers, see e.g. [17–19]. When voids form inside the amorphous phase of an un-filled semi-crystalline polymer, the void morphology is constrained by the comparatively stiff crystalline lamellae of the microstructure. Initiated as penny-shaped voids, these voids grow into barrel shaped cavities upon further deformation. However, when filler particles are added to the polymer to improve mechanical or processing properties [20–23], the voids may also form around the particles due to separation of the particles from the matrix at the interface, see e.g. [15], or inside the particles themselves [21,22,24,25].

An increased stress triaxiality ratio is commonly associated with higher degrees of void growth in thermoplastics such as mineral filled PVC [14,26], PA11 [27], HDPE [26], and PVDF [28,29]. Conversely, by increasing the ambient temperature in uniaxial tensile tests of PVDF specimens, less void growth [12,16] was observed. Also, as the nucleation of voids decreases at higher temperatures, PVDF exhibits a tendency to turn translucent or transparent during stretching [12].

Studying deformation-induced void nucleation and growth in thermoplastics is challenging due to these materials' rate-dependent behaviour as well as the wide range of relevant length scales. Non-intrusive techniques such as small-angle X-ray scattering (SAXS) [30,31] and X-ray computed tomography (XCT) [18,19,27,32] have been extensively used to study void formation and growth in thermoplastics on the micro- and nanoscale. However, these techniques are often limited to *ex situ* measurements and are typically experimentally demanding, making such techniques less suited to studies assessing a wide range of parameters. A convenient way of studying the evolution of void growth in a deforming polymer specimen is to estimate the degree of void growth from the macroscopic volume strain. The volume strain can be estimated for a cross section of the specimen based on surface deformation measurements using methods such as digital image correlation (DIC) [33]. However, this approach relies on assumptions regarding the deformation field inside the specimen during deformation, limiting the technique to macroscopic qualitative assessments [19,32]. When the morphology of voids after failure is of primary interest, imaging cross sections of material specimens by scanning electron microscopy (SEM) can provide detailed insight into the deformation mechanisms involved.

This study combines mechanical tests of different specimen geometries deformed to large strains with analyses of the deformed material morphology on the microscale, aiming for a better understanding of the large-strain behaviour of PVDF under different loading conditions relevant for engineering applications. To investigate the thermo-viscoplastic material behaviour, uniaxial tensile tests were performed at different ambient temperatures and strain rates. Additionally, the influence of the stress triaxiality on the material response was studied using axisymmetric notched tensile specimens with different notch radii and compression specimens. Local surface deformations were measured using DIC, allowing the net axial stress and volume strain response to be determined. For the analyses of the material morphology, the cross section of failed specimens was imaged by SEM.

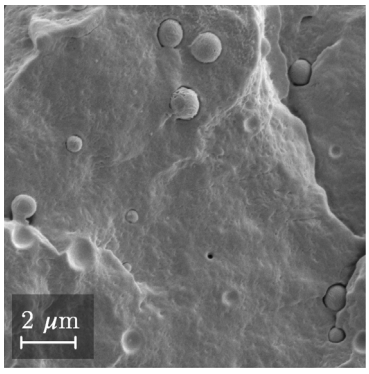

Fig. 1. SEM micrograph of an undeformed PVDF sample showing the embedded PE particles. The imaged surface was obtained by cryogenically cracking an undeformed material sample.

2. Material & methods

The aim of the experimental study was to investigate the large-strain response of a commercial PVDF grade at different temperatures, strain rates and stress triaxialities relevant for engineering applications.

2.1. Material

The PVDF material was provided as a section of an extruded pipe with a nominal outer diameter of 100 mm and a nominal wall thickness of 10 mm. This particular grade of PVDF is marketed as a copolymer featuring a high viscosity of the melt flow suited for piping applications where the material has to withstand high temperatures and high pressures. The glass transition temperature and the melting temperature are specified by the manufacturer as −40 °C and 170 °C, respectively. The morphology of the material was assessed by SEM and is shown in Fig. 1. The PVDF matrix material contained a low fraction of spherical particles, and results from differential scanning calorimetry (DSC) and energy dispersive X-ray spectroscopy (EDX) strongly indicate that the particles consisted of poly-ethylene (PE). These particles had varying sizes in the order of 1 μm and appeared to be evenly dispersed throughout the material volume.

2.2. Specimen specifications

The five different types of axisymmetric specimens employed in this study were one uniaxial tension specimen, three notched tension specimens featuring different notch radii, and one cylindrical compression specimen. The geometries were chosen to assess the material response in stress states spanning from compression to higher tension-dominated stress triaxialities. The specimens were manufactured using a turning lathe, aligning the longitudinal l-axis of the specimen with the longitudinal axis of the pipe, see Fig. 2. The radial direction $\vec{e}_r$ of the pipe was indicated on the specimens, allowing for identification of possible anisotropy of the material behaviour. The tension specimens all featured threaded ends for fixation to the testing machine.

The geometry of the uniaxial tension (UT) specimens is shown in Fig. 3. To vary the initial stress triaxiality ratio in the tensile tests, axisymmetric notched tension (NT) specimens with three different notch radii R of 2 mm, 5 mm, and 20 mm, referred to as NT2, NT5, and NT20, respectively, were used. The dimensions of the three NT specimens are given in Fig. 4.

The stress triaxiality ratio η is given by

$$\eta = \frac{\sigma_m}{\sigma_e}, \tag{1}$$

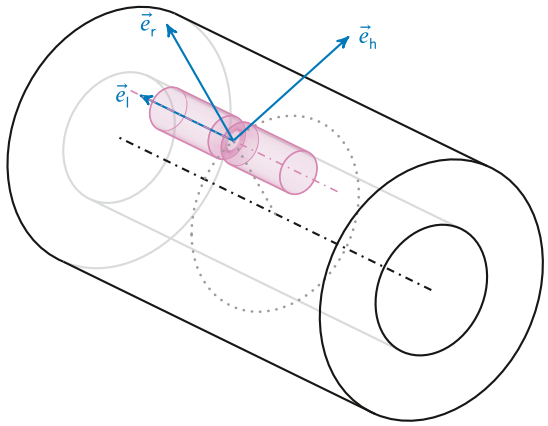

Fig. 2. Illustration of the extruded pipe and orientation of extracted specimen with corresponding coordinate system $\{\vec{e}_l, \vec{e}_r, \vec{e}_h\}$.

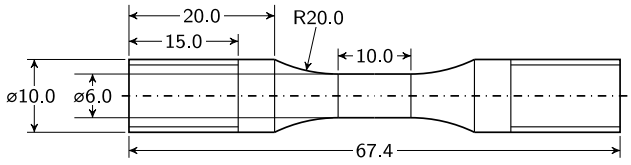

Fig. 3. Geometry of UT specimens. All dimensions in mm.

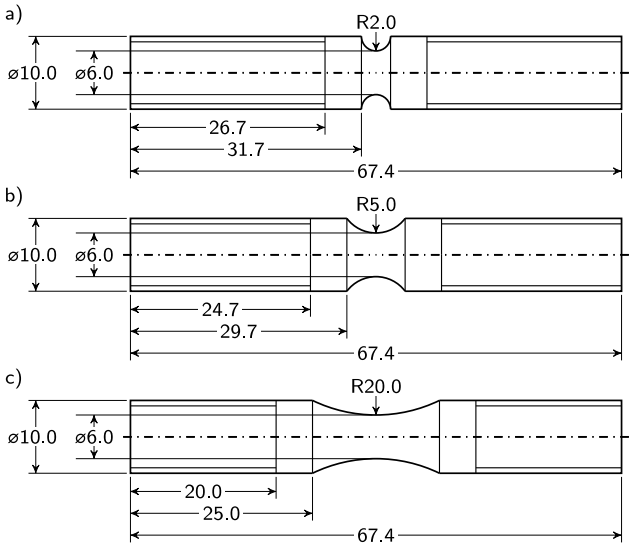

Fig. 4. Geometry of the NT specimens featuring different notch radii: (a) NT2, (b) NT5, (c) NT20. All dimensions in mm.

where σ_m denotes the hydrostatic stress and σ_e is the von Mises equivalent stress. Under the assumption of linear elastic material behaviour, Ognedal et al. [26] used finite element simulations to determine the initial stress triaxiality in specimens featuring the same notch radii and diameters. According to these simulations, a notch radius R of 20 mm, 5 mm, or 2 mm yields an initial stress triaxiality ratio η in the centre of the specimen of approximately 0.4, 0.6, and 0.8, respectively [26].

The uniaxial compression (UC) specimens were of cylindrical shape with a diameter and length of 6 mm.

To facilitate the process of image correlation, a random speckle pattern was applied to the surface of the specimens. For the specimens tested at or above room temperature, the speckle pattern was applied using an airbrush and black paint, whereas white grease and a black powder were used to create a speckle on the specimens tested at lower temperatures [34].

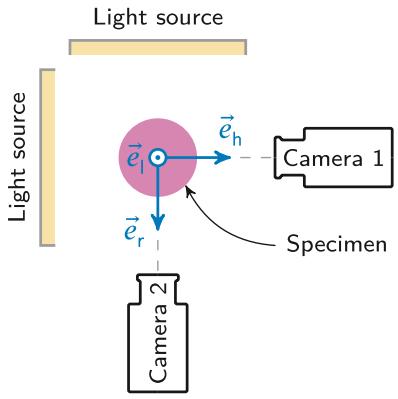

Fig. 5. Schematic drawing of top view onto the experimental setup.

Table 1
Crosshead velocities, nominal strain rates, and testing machines used in the UT, NT, and UC tests.

Specimen type	Nominal strain rate $\dot{e}$ [s^{-1}]	Crosshead velocity $\dot{u}$ [mm s^{-1}]	Gauge section length [mm]	Testing machine
UT	0.005	0.05	10.0	Instron® 5944
UT	0.1	1.0	10.0	Instron® 5944
UT	1.0	10.0	10.0	Instron® 5944
NT20	0.005	0.087	17.4	Instron® 5944
NT5	0.0016	0.0125	8.0	Instron® 5944
NT2	0.0013	0.005	4.0	Instron® 5944
UC	0.005	0.03	6.0	Instron® 5566

2.3. Experimental setup

The uniaxial tensile tests using UT and NT specimens were carried out employing an Instron® 5944 testing machine featuring a load capacity of 2 kN equipped with a 2 kN load cell. Additionally, the deformation of the specimen's gauge section was measured using a 2D DIC system equipped with two orthogonally positioned cameras. A detailed description of the DIC setup is given in Section 2.4. In all UT and NT experiments, the testing machine's fixation mechanism comprised of two threaded grippers in which the threaded ends of the specimens were mounted. The crosshead velocities of the tensile test machine were chosen such that the desired nominal strain rate with respect to the initial length of the specimen gauge section was obtained. Three successful repetitions of each experiment were carried out, to assess the reproducibility of the results.

2.3.1. UT tests at various strain rates

The material behaviour under uniaxial tension was investigated for three nominal strain rates at room temperature (T = 25 °C). Nominal strain rates $\dot{e}$ of 0.005 s^{-1}, 0.1 s^{-1}, and 1 s^{-1} were targeted in this study, representing strain rates relevant for a wide range of engineering applications. The lowest strain rate $\dot{e}$ = 0.005 s^{-1} was assumed small enough to not cause self-heating of the specimens, whereas the elevated strain rates were anticipated to cause notable self-heating. Based on a gauge length of 10 mm, crosshead velocities $\dot{u}$ of 0.05 mm s^{-1}, 1.00 mm s^{-1} and 10.00 mm s^{-1} were applied (see Table 1).

To monitor the self-heating of the specimens deformed at nominal strain rates $\dot{e}$ of 0.1 s^{-1} and 1.0 s^{-1}, the temperature of the specimen surface was measured using a FLIR SC 7500 infrared (IR) camera. In each of these tests, the temperature difference was measured on a portion of the specimen surface at the centre of the gauge section

and spatially averaged to obtain a scalar value. The temperature field was approximately constant within the region where the average was calculated. To account for the increasing crosshead displacement and longitudinal strain, respectively, and monitor the same region of the specimen surface, the area of measurement was adjusted continuously.

2.3.2. UT tests at various temperatures

The influence of ambient temperature on the mechanical response of the material was investigated for six different temperatures $T = \{-20, 4, 25, 60, 80, 100\}$ °C. This temperature range was chosen to span from temperatures approaching the glass transition temperature of PVDF up to temperatures relevant for high-temperature applications. To avoid self-heating of the specimens, the tests were carried out using a crosshead velocity $\dot{u}$ of 0.05 mm s^{-1} and a nominal strain rate $\dot{e}$ of 0.005 s^{-1}. In order to control the ambient temperature, a transparent temperature chamber was added to the experimental setup shown in Fig. 5. The chamber, also used in previous studies [34,35], was constructed in a manner such that two cameras could be positioned perpendicular to each other and the specimens' longitudinal axis to monitor the deformation. Additionally, the chamber featured a slit such that the thermal camera used for the UT strain rate tests could be employed to monitor the temperature of the specimen surface. In order to ensure a homogeneous temperature in the specimens, the specimens tested at 60 °C, 80 °C and 100 °C were thermally conditioned within the chamber for 45 min before testing. The specimens deformed at −20 °C and 4 °C were conditioned for approximately 30 min.

2.3.3. NT tests

To calculate the nominal strain rate in the NT tests, the notched region of the specimens was taken as the length of the gauge section. Thus, different crosshead velocities were used to account for the different specimen geometries. In the case of the NT20 specimens, a crosshead velocity $\dot{u} = 0.087$ mm s^{-1} was used. In relation to the length of the notched specimen section of 17.44 mm, this crosshead velocity yielded a nominal strain rate $\dot{e} = 0.005$ s^{-1}. In the case of the NT5 and NT2 specimens, crosshead velocity $\dot{u}$ of 0.0125 mm s^{-1} and 0.005 mm s^{-1} were used. Taking into account the respective gauge section lengths of 8 mm (NT5) and 4 mm (NT2), resulted in nominal strain rates $\dot{e}$ of 0.0016 s^{-1} and 0.0013 s^{-1} (see Table 1).

2.3.4. UC tests

For the uniaxial compression (UC) tests, an Instron® 5566 testing machine featuring a load capacity of 10 kN equipped with a 10 kN load cell was used. Targeting the quasi-static nominal strain rate $\dot{e}$ of 0.005 s^{-1} used in the UT tests, the crosshead velocity $\dot{u}$ was set to 0.03 mm s^{-1} (see Table 1). The UC tests were carried out up to a final machine displacement u of 4.8 mm or a magnitude of the longitudinal engineering strain $|\varepsilon_l|$ of 0.8, respectively.

2.4. Calculation of net axial stress and logarithmic strain

To estimate the net axial stress *vs.* logarithmic strain response of the material, the local surface deformations in the notch root of the tensile specimens were measured using 2D DIC. The gauge section of the specimens was imaged during deformation using two orthogonally positioned 12MP Basler acA4112-30um cameras. The cameras were equipped with Samyang 100 mm f/2.8 ED UMC MACRO lenses for the NT2 and NT5 tests, whereas Kowa 50 mm LM50FC24M lenses were used for NT20 and UT experiments. The two cameras were oriented coaxially to the hoop direction $\vec{e}_h$ and radial direction $\vec{e}_r$ of the pipe, see Fig. 2, allowing potential material anisotropy to be identified. DIC was performed using the finite element based DIC code eCorr, employing Q8 elements. To ensure that local strains were fully resolved, the size of the finite elements was successively reduced until no further increase in local strain was observed.

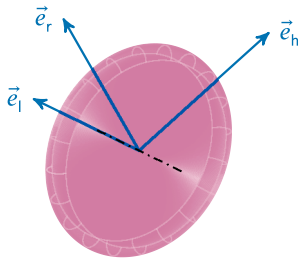

Fig. 6. Illustration of platelet shaped UC specimen (post deformation) and orientation of coordinate system.

The deformation of the minimum cross section of the specimens was quantified through the stretch ratios λ_l, λ_r and λ_h, where the subscripts denote the longitudinal direction $\vec{e}_l$, radial direction $\vec{e}_r$, and hoop direction $\vec{e}_h$ of the extruded pipe, respectively (see Fig. 2). The stretch ratios were determined as the average of the values extracted along a horizontal line spanning the visible circumference of the notch, see Johnsen et al. [35] for a detailed discussion.

Assuming that the minimum cross section of the specimens is accurately described by an ellipse with minor and major axes being coaxial with the r and h axes, the net axial stress σ is calculated as

$$\sigma = \frac{F}{A} = \frac{F}{A_0 \lambda_r \lambda_h}, \tag{2}$$

where F denotes the reaction force measured by the load cell and A is the current area of the minimum cross section.

A_0 is the initial specimen cross section which was determined based on the diameter of the specimen prior to testing, measured using a calliper. Similarly, the logarithmic longitudinal strain was calculated as

$$\varepsilon_l = \ln(\lambda_l). \tag{3}$$

Assuming that the strain field within the minimum cross section is homogeneous, the logarithmic volume strain was calculated as

$$\varepsilon_v = \ln(\lambda_l \lambda_r \lambda_h). \tag{4}$$

2.5. SEM sample preparation

To gain insight into the void morphology of failed specimens, the specimens were cryogenically cracked and the resulting fracture surfaces imaged using SEM. In the case of the UT and NT tests, the samples were extracted from the necked sections of the ruptured specimen halves and cracked along their l-axis. To investigate the morphology following a UC test, one whole plastically deformed and therefore platelet shaped specimen was cracked open along its rh-plane (see Fig. 6). To cryogenically crack open the samples, they were first immersed in liquid nitrogen for 40 min and thus cooled down to approximately −196 °C. After removal, each sample was cracked open using a sharp blade and a hammer. The samples were subsequently gold coated using sputter deposition to prevent electrostatic charging of the non-conductive material during SEM. The image acquisition was carried out employing a Zeiss® SUPRA® 55 VP field emission scanning microscope using an acceleration voltage of 10 kV.

3. Results

The mechanical response of the material in terms of net axial stress *vs.* logarithmic strain plots and corresponding volume strain plots are shown for different strain rates, temperatures, and stress triaxialities in the following section. To illustrate the repeatability of the experiments, the results from repeat tests as well as the mean value of all repeat tests are presented. To corroborate on the mechanisms governing the volume strain response, SEM images showing the void morphology of selected cross sections within failed specimens are presented and discussed.

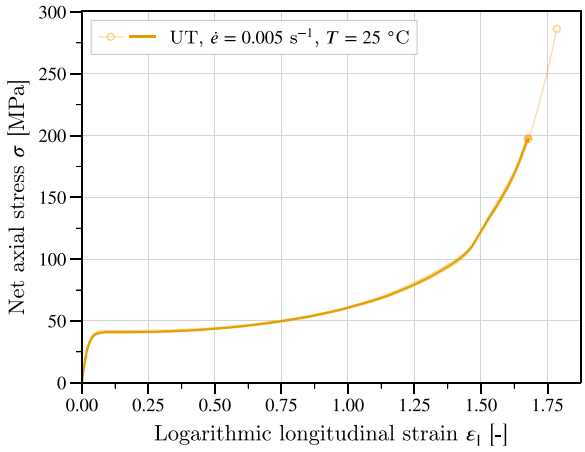

Fig. 7. Net axial stress response in uniaxial tensile tests deformed at a nominal strain rate of $\dot{e} = 0.005\,s^{-1}$ and room temperature ($T = 25\ °C$).

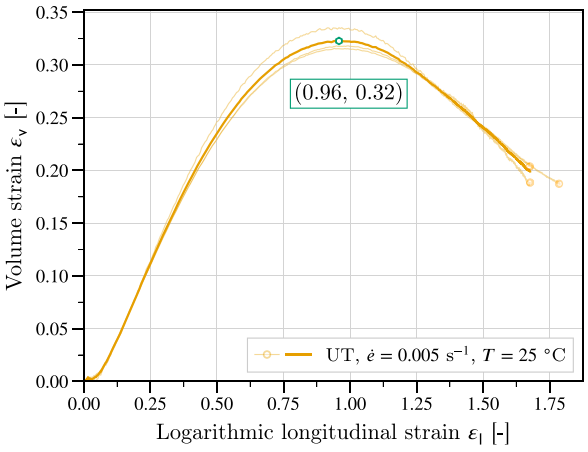

Fig. 8. Volume strain response in uniaxial tensile tests deformed at a nominal strain rate $\dot{e} = 0.005\,s^{-1}$ and room temperature ($T = 25\ °C$).

3.1. Uniaxial tensile tests

The net axial stress *vs.* logarithmic strain response and corresponding volume strain evolution for the UT tests carried out at room temperature and a nominal strain rate $\dot{e}$ of $0.005\,s^{-1}$ are shown in Figs. 7 and 8, respectively. Based on the similarity of the response from repeat tests, the repeatability of the experiments appears to be satisfactory for the purpose of this study. The material exhibited a linear elastic response up to a logarithmic strain of approximately 0.05 (see Fig. 7), followed by a transition to almost perfect plasticity. The onset of yield manifests itself in the volume strain ε_v through a pronounced uptake of the dilation (see Fig. 8). Up to a strain ε_l of approximately 0.25, the net axial stress level remains constant without pronounced softening or hardening. In the same range of the longitudinal strain, the volume strain ε_v exhibits its steepest increase (see Fig. 8). For strains ε_l larger than 0.25, the stress response shows progressive rehardening up to failure at a strain ε_l of approximately 1.6. The volume strain was found to increase up to a strain ε_l of 0.96, reaching an average maximum of 0.32 (Fig. 8). However, with the continuation of the deformation, the volume strain decreased to about 0.2 at failure. Fig. 9a shows the morphology in the cross section of a UT specimen post failure. Despite observing a decrease in the macroscopic volume strain ε_v prior to failure, a significant void volume fraction was found. The largest voids developed around the PE particles that retained their spherical shape. However, the majority of the voids was found to have nucleated in the PVDF matrix phase. All voids were highly elongated along the principal stress direction (see Fig. 9a).

3.1.1. Impact of the strain rate on the material response

To investigate the material's viscoplastic properties, additional UT tests were performed at elevated strain rates $\dot{e} = 0.1\,s^{-1}$ and $\dot{e} = 1.0\,s^{-1}$ at room temperature ($T = 25\ °C$) while measuring the temperature of the specimen surface. The net axial stress and volume strain *vs.* logarithmic strain responses of these tests as well as the quasi-static UT tests are shown in Figs. 10 and 11, respectively. Fig. 12 shows the average net axial stress response of the UT tests at each strain rate up to a longitudinal logarithmic strain ε_l of 0.25. For an increasing strain rate, the net axial stress at the onset of yielding was found to increase. Defining the yield stress σ_0 as the point fulfilling $d\sigma/d\varepsilon_l = 0$, values ranged from 41.0 MPa for $\dot{e} = 0.005\,s^{-1}$ to 50.0 MPa for $\dot{e} = 1.0\,s^{-1}$ (see Fig. 12). In comparison to the quasi-static case ($\dot{e} = 0.005\,s^{-1}$), the yield stress increased by 11% for the strain rate $\dot{e} = 0.1\,s^{-1}$ and by 22% in the case of $\dot{e} = 1.0\,s^{-1}$ (see Fig. 12).

For an increasing strain rate, the material's stress response featured an increasingly pronounced softening upon yield which was not present in the case of the slowest UT tests (see Fig. 12). The slow tests exhibited the greatest amount of progressive rehardening and thus ultimate strength (see Fig. 10). The net axial stress curves of the tests at the intermediate strain rate $\dot{e} = 0.1\,s^{-1}$ shown in Fig. 10 feature a sudden stark increase in modulus at a longitudinal strain ε_l of approximately 1.6. In the case of these UT tests, the neck propagated out of the gauge section and into the specimen shoulders (see Appendix). As a result, the observed stark increase of the hardening in the corresponding net axial stress curves is due to plastic rehardening of the material outside of the gauge section where also the cross-sectional area increases. Therefore, this apparent rehardening cannot be considered part of the true material response and is disregarded.

Regarding the volume strain responses shown in Fig. 11, an increasing degree of plastic dilation with an increasing strain rate was found. However, the difference between the two higher strain rates was within the spread of the individual test results (see Fig. 11). Comparing the quasi-static case ($\dot{e} = 0.005\,s^{-1}$) with the two elevated strain rates ($\dot{e} = 0.01\,s^{-1}$ and $\dot{e} = 0.1\,s^{-1}$), the maximum volume strain shifted to larger longitudinal strains for the elevated strain rates (see Fig. 11).

Fig. 13 shows the logarithmic longitudinal strain rate $\dot{\varepsilon}_l$ as a function of the logarithmic longitudinal strain ε_l in the uniaxial tensile tests at the three strain rates investigated. In the elastic range of all curves, the local logarithmic longitudinal strain rate $\dot{\varepsilon}_l$ does not match the nominal strain rate values. This is a result of elastic deformations outside of the specimens' gauge section which was used as the reference length for the nominal strain rates. After the onset of plastic flow and therefore localisation of the deformation in the gauge section, the nominal strain rate was reasonably well approximated for all three crosshead velocities (see Fig. 13). With the onset of neck propagation, the logarithmic strain rates started to increase and exceed the nominal strain rate values in all curves. This trend continued until the onset of neck propagation, resulting in a decline of the observed logarithmic longitudinal strain rates.

The temperature difference between the specimen surface and the ambient temperature of 25 °C for both elevated strain rates is shown in Fig. 14. The measured temperatures briefly declined at small strains up to approximately 0.15 as a result of the thermoelastic effect [36]. Afterwards, the temperature increased for both strain rates. This temperature increase was more pronounced in the case of the higher strain rate $\dot{e} = 1.0\,s^{-1}$, reaching a maximum temperature difference $\Delta T_{max} = 52.8\,K$ (see Fig. 14) as opposed to a maximum temperature $\Delta T_{max} = 34.1\,K$ in the case of the lower strain rate $\dot{e} = 0.1\,s^{-1}$.

For the specimens deformed at the lower strain rate $\dot{e} = 0.1\,s^{-1}$, the temperature difference steeply declined before final failure (see Fig. 14) due to heat conduction within the specimen. For large overall

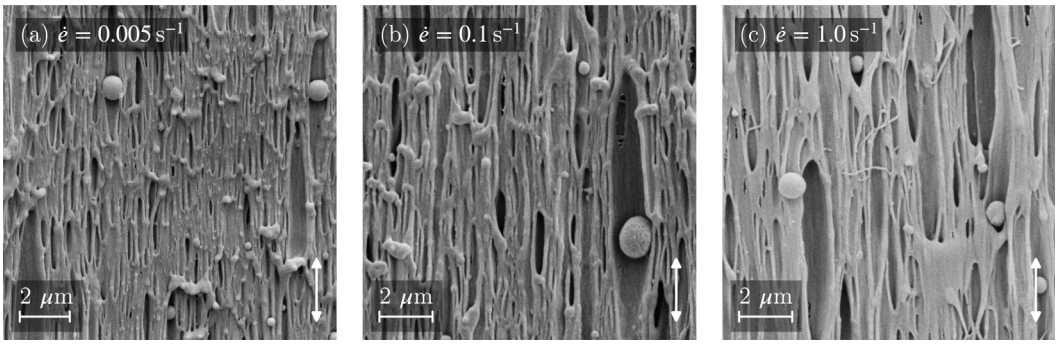

Fig. 9. SEM micrographs of morphology in necked region of uniaxial tensile specimens (post failure) tested at room temperature (T = 25 °C) and a nominal strain rate of (a) $\dot{e} = 0.005\,s^{-1}$, (b) $\dot{e} = 0.1\,s^{-1}$, and (c) $\dot{e} = 1.0\,s^{-1}$. The direction of the tensile stress is indicated through the white arrow.

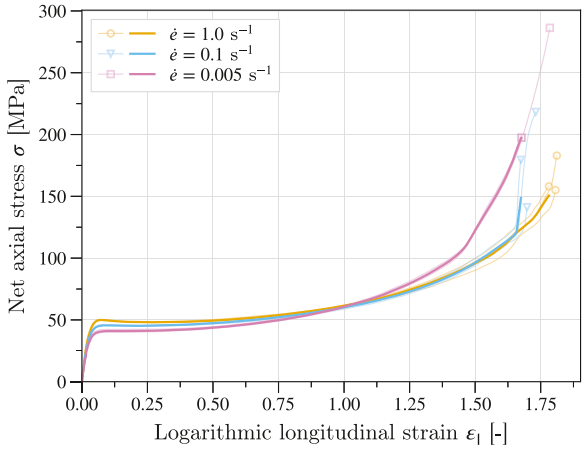

Fig. 10. Strain rate dependency of the net axial stress response in uniaxial tensile tests at room temperature (T = 25 °C).

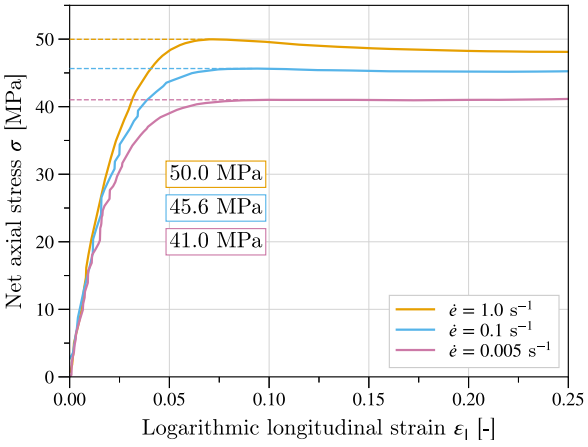

Fig. 12. Strain rate dependency of the net axial stress at the onset of yielding in uniaxial tensile tests at room temperature (T = 25 °C).

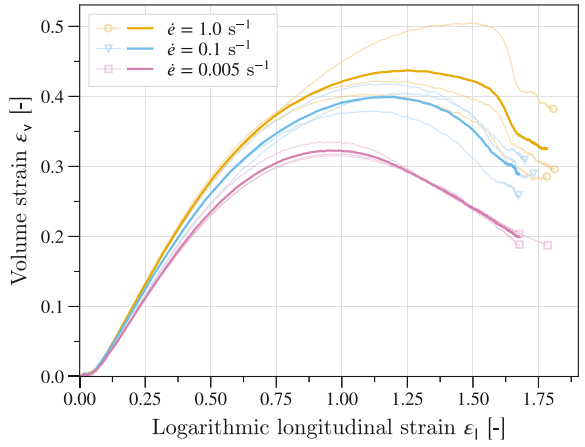

Fig. 11. Strain rate dependency of the volume strain response in uniaxial tensile tests at room temperature (T = 25 °C).

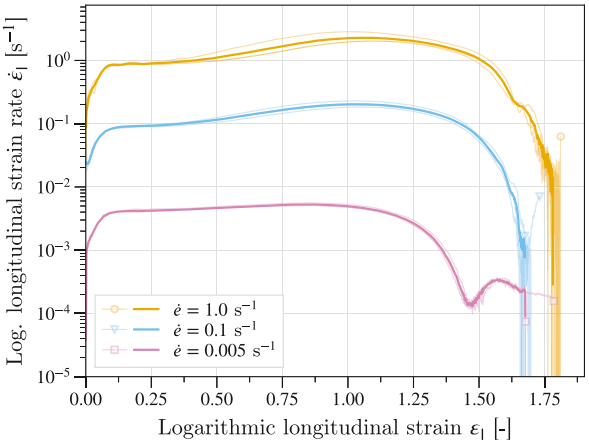

Fig. 13. Longitudinal logarithmic strain rate $\dot{\varepsilon}_l$ *vs.* longitudinal logarithmic strain ε_l from uniaxial tensile tests for the three strain rates investigated at room temperature (T = 25 °C).

displacements, the deformation mainly progressed outside the initial specimen gauge section centre where the temperature was measured. Therefore, deformation and dissipation in the gauge section stalled as a result (see also Appendix). Long test durations due to the relatively low strain rate allowed for the self-generated heat to be conducted within the specimen, resulting in a decreasing temperature at the point of measurement. Fig. 9b and c show the post-failure morphology in the cross section of UT specimens tested at a nominal strain rate of $\dot{e} = 0.1\,s^{-1}$ and $\dot{e} = 1.0\,s^{-1}$, respectively. Both morphologies feature a high void volume fraction with voids that are highly elongated along the principal stress direction, similar to what was found in the case of a nominal strain rate $\dot{e} = 0.005\,s^{-1}$.

3.1.2. *Impact of the ambient temperature on the material response*

The stress–strain response of the UT tests at different ambient temperatures is shown in Fig. 15 with the corresponding volume strain behaviour being shown in Fig. 16. The temperature control system used in tests at elevated temperature introduced fluctuations in the

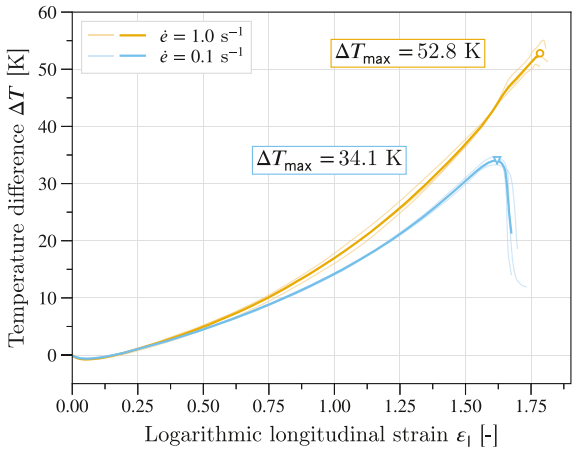

Fig. 14. Evolution of the temperature change with respect to the ambient temperature (T = 25 °C) on the surface of UT specimens in the gauge section for elevated strain rates.

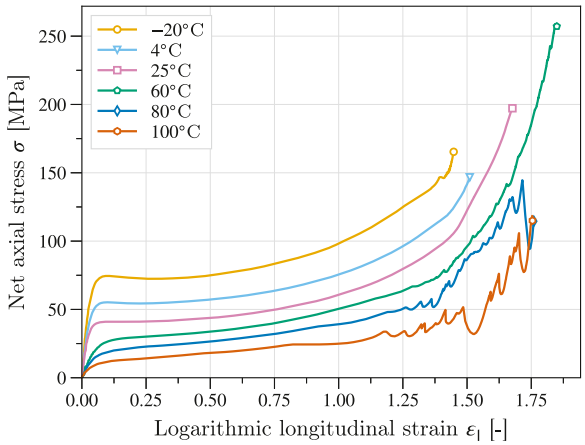

Fig. 15. Temperature dependency of the net axial stress response in uniaxial tensile tests carried out at a nominal strain rate $\dot{e} = 0.005\,s^{-1}$.

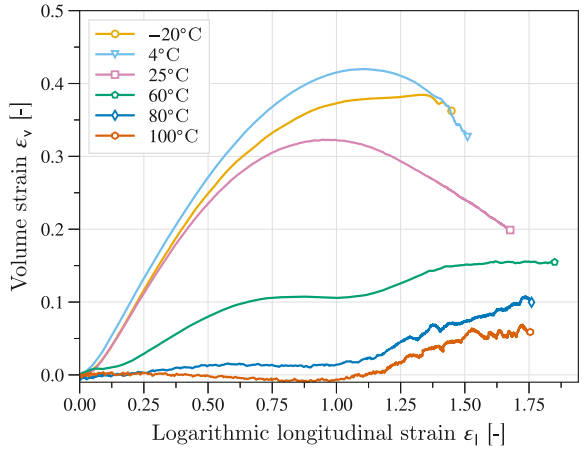

Fig. 16. Temperature dependency of the volume strain response in uniaxial tensile tests carried out at a nominal strain rate $\dot{e} = 0.005\,s^{-1}$.

chamber temperature of about ±5 °C over the total duration of the tests. Consequently, these temperature fluctuations have to be taken into account when interpreting the results from the high temperature tests.

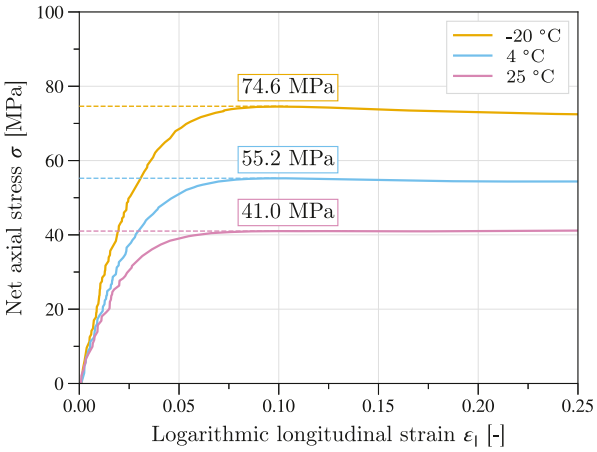

Fig. 17. Temperature dependency of the net axial stress at the onset of yielding σ_0 in uniaxial tensile tests at temperatures of 25 °C, 4 °C, and −20 °C.

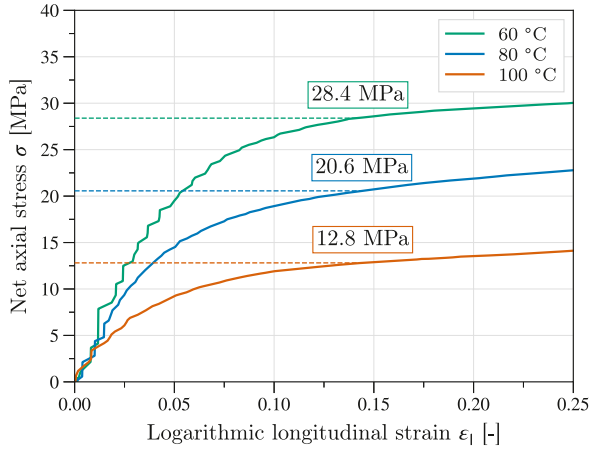

Fig. 18. Temperature dependency of the net axial stress at the onset of yielding σ_0 in uniaxial tensile tests at temperatures of 60 °C, 80 °C, and 100 °C.

The overall stress level was found to increase with decreasing temperature (see Fig. 15). Considering the lower temperature range between −20 °C and 25 °C, the net axial stress curves were found to be approximately self-similar from the onset of yield up to a logarithmic strain of approximately 1.4. In this temperature range, the yield stress σ_0 increased from 41.0 MPa at room temperature (T = 25 °C) to 74.6 MPa at a temperature of −20 °C and to σ_y = 55.2 MPa at 4 °C (see Fig. 17).

In the upper temperature range comprising temperatures $T \geq 60$ °C, both the yield stress and the initial modulus were found to decrease. At these temperatures, no plateau stress could be determined (see Fig. 15). Based on the longitudinal strains corresponding with the plateau stresses in the uniaxial tensile tests at lower temperatures, the stress at a longitudinal strain $\varepsilon_l = 0.15$ was taken as the yield stress in these cases. At a temperature of 60 °C, this yield stress amounted to 28.4 MPa. The yield stress decreased to 20.6 MPa at a temperature of 80 °C and 12.8 MPa at a temperature of 100 °C, respectively (see Fig. 18).

The volume strain was observed to decrease with increasing temperature (see Fig. 16). An exception from this trend is the plastic dilation measured at a temperature of −20 °C which was lower than that found for T = 4 °C. Hence, the greatest plastic dilation with a maximum value of 0.42 was found for a temperature of 4 °C.

For the tests carried out in the lower temperature range ($T \leq$ 25 °C), a pronounced increase of the volume strain after onset of yielding was found. However, the volume strain responses of these tests

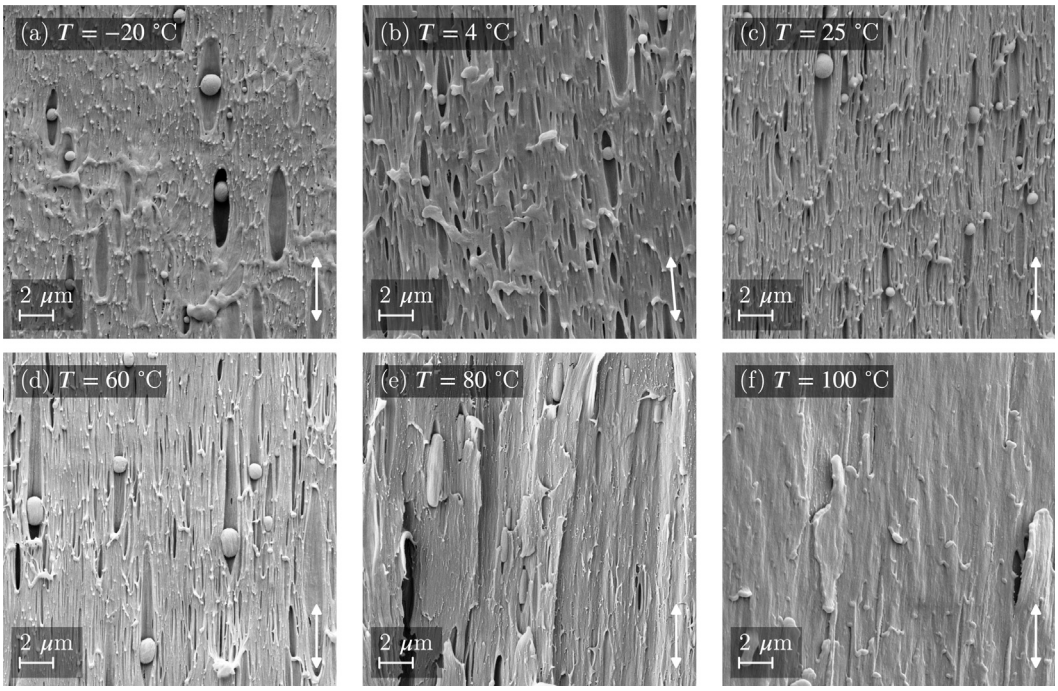

Fig. 19. Impact of the ambient temperature on the morphology in UT specimens (post failure) for temperatures of (a) $T = -20$ °C, (b) $T = 4$ °C, (c) $T = 25$ °C, (d) $T = 60$ °C, (e) $T = 80$ °C, and (f) $T = 100$ °C. The white arrows indicate the tensile stress direction.

exhibit a regressive trend with ongoing deformation for strains $\varepsilon_l \geq 0.5$. Considering the tests at temperatures $T = 4$ °C and $T = 25$ °C, the volume strain response features a maximum and subsequent decrease. Regarding the large-strain volume strain response for a temperature of −20 °C, the growth subsided as well yet only a small decrease was found until failure.

In the upper temperature range ($T \geq 60$ °C), the volume strain was reduced compared to the results in the lower temperature range. Whereas in the case of a temperature of 60 °C, an increasing volume strain upon plastic deformation was found, no such increase considering temperatures $T = 80$ °C and $T = 100$ °C was observed. With temperature fluctuations in mind, the uptake in the volume strain response of the tests carried out at temperatures $T \geq 60$ °C, setting on at a longitudinal strain ε_l of approximately 1.0, is treated as at measurement uncertainty and disregarded in the following discussion.

The mechanisms on the microscale causing the macroscopic volume strain are reflected in the SEM micrographs shown in Fig. 19. The micrographs of samples from tests carried out at temperatures $T \leq 60$ °C, shown in Fig. 19a, b, c, and d, all show extensive cavitation and void growth. In agreement with the volume strain measurements, the visual impression is that the samples from the tests at temperatures $T \leq 25$ °C, featured a higher overall porosity than the sample extracted from the specimen subjected to a temperature $T = 60$ °C. Furthermore, for temperatures of 25 °C, 4 °C, and −20 °C, the PE particles remained spherical even after the extensive deformation of the matrix.

Fig. 19e shows the heterogeneous microstructure of a specimen tested at $T = 80$ °C, featuring a low porosity. However, in this case, the particles apparently deformed with the PVDF matrix material and only detached from the matrix at their tips in the tensile direction. Voids stemming from nucleation were found to be sparse and small in relation to those occurring at samples from tests conducted at lower temperatures. The micrograph showing the sample from the test carried out at $T = 100$ °C does not show any porosity (see Fig. 19f). Also, the morphology of the sample proved to be homogeneous without particles or voids. It should be noted that the specimens deformed at $T = 100$ °C turned translucent during deformation instead of displaying stress-whitening.

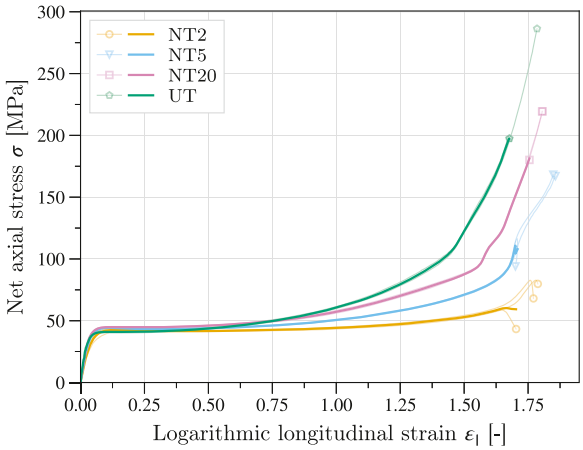

Fig. 20. Impact of the stress triaxiality on the stress–strain response at room temperature ($T = 25$ °C).

3.2. NT tests and the impact of the stress triaxiality ratio

To investigate the material's susceptibility to void formation and growth when subjected to an elevated stress triaxiality, tensile tests on NT specimens featuring different notch radii were carried out. The net axial stress *vs.* logarithmic strain responses of the NT tests, with the quasi-static UT tests added for comparison, are shown in Fig. 20 and the average responses of repeat tests up to a strain ε_l of 0.25 are depicted in Fig. 21.

The longitudinal stress at the onset of yielding was found to not vary significantly with the notch radius or stress triaxiality ratio, respectively. Furthermore, the longitudinal stress response up to a logarithmic strain ε_l of approximately 0.5 was found to be similar across all notch radii. Only for further increased strain, a decreasing degree of hardening with respect to the longitudinal stress was observed for a decreasing notch radius.

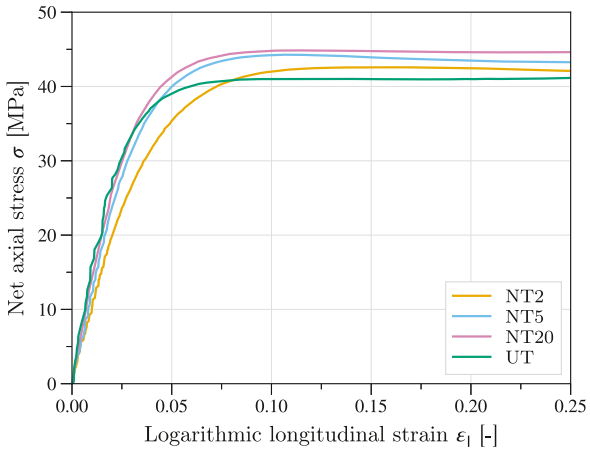

Fig. 21. Longitudinal stress at the onset of yielding for different notch radii.

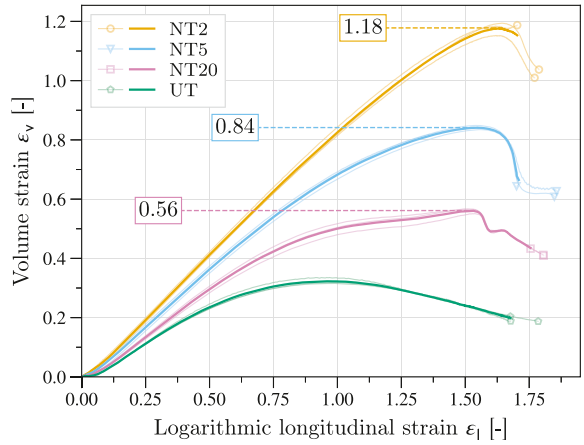

Fig. 22. Impact of the stress triaxiality on the volume strain response at room temperature ($T = 25$ °C).

The volume strain responses of the NT tests as well as the quasi-static UT tests are shown in Fig. 22. For all specimens, extensive plastic dilation was observed with a decreasing notch radius resulting in an increasing volume strain. The maximum average volume strain in the UT tests, i.e. for a stress triaxiality ratio $\eta = 1/3$, amounted to $\varepsilon_v = 0.32$ (see Fig. 8). For the NT20 tests, featuring an initial stress triaxiality ratio $\eta = 0.4$, the maximum volume strain increased to 0.56. A further increased maximum of the volume strain ε_v of 0.84 was found in the case of the NT5 specimens ($\eta = 0.6$). During the NT2 tests ($\eta = 0.8$), the volume strain ε_v reached a maximum of 1.18. SEM images showing the void morphology of samples extracted from the NT specimens are shown in Fig. 23. The micrographs show an apparently increasing porosity for a decreasing notch radius, conforming to the increased volume strain. The void morphology of the NT20 sample (see Fig. 23a) was similar to the UT sample with highly elongated voids. The NT5 and NT2 samples both featured an even higher porosity (see Fig. 23b and c). While the elongation of the voids decreased with an decreasing notch radius, their diameter increased. Furthermore, the thickness of the ligament between voids decreased with a decreasing notch radius.

3.3. Uniaxial compression tests

The force *vs.* machine displacement responses of the quasi-static uniaxial compression tests are shown in Fig. 24. The UC specimens exhibited barrelling, did not crack, and retained a platelet shape after the experiments. Due to the barrelling and complex interaction between the specimen and the fixture through a varying contact surface area and frictional effects, the UC tests were only considered for small strains to obtain the yield stress. The magnitude of the average net axial stress *vs.* the magnitude of engineering strain response under compression and tension is shown in Fig. 25. The average magnitude of the yield stress under compression $|\sigma_{0,c}|$ was 53.24 MPa, being increased by 30% over the average magnitude of the yield stress in tension $|\sigma_{0,t}|$ of 41.02 MPa. Hence, a yield stress ratio $|\sigma_{0,c}|/|\sigma_{0,t}| = 1.30$ was determined, further demonstrating that the material is highly pressure sensitive.

The surface morphology of a material sample extracted from the centre of the deformed specimen is shown in Fig. 26. Here, no cavitation, particle–matrix separation, and consequentially no porosity was observed. However, an increase of the diameter of the particles prior and post deformation (see Figs. 1 and 26) indicated that the particles had been plastically deformed into platelets.

Table 2
Material parameters in the Ree–Eyring model (Eq. (5)).

V_α [nm^3]	ΔH_α [kJ/mol]	$\dot{e}_{0,\alpha}$ [s^{-1}]	V_β [nm^3]	ΔH_β [kJ/mol]	$\dot{e}_{0,\beta}$ [s^{-1}]
2.69	248.40	$9.56 \cdot 10^{29}$	6.25	496.21	$4.72 \cdot 10^{86}$

4. Discussion

Strain rate, ambient temperature, and stress triaxiality were found to have a pronounced impact on the net axial stress *vs.* logarithmic strain response of PVDF as well as on the degree of void growth.

The stress level was observed to increase with increasing strain rate or decreasing temperature, respectively, demonstrating that the material adheres to the equivalence principle. Accordingly, a drop in ambient temperature impacts the material response similarly as an increased strain rate [37–39].

Fig. 27 shows the dependence of the yield stress σ_0 on the nominal strain rate $\dot{e}$ and temperature T in uniaxial tensile tests, complemented by a fitted Ree–Eyring model. The Ree–Eyring flow theory [40] describes the rate and temperature dependence of a material's yield stress σ_0 as given by

$$\sigma_0 = \sum_{x=\alpha,\beta} \frac{k_B \theta}{V_x} \operatorname{arcsinh}\left(\frac{\dot{e}}{\dot{e}_{0,x}} \exp\left[\frac{\Delta H_x}{R\theta}\right]\right), \tag{5}$$

where α and β denote two material-specific relaxation processes each associated with an activation volume V_x, a reference strain rate $\dot{e}_{0,x}$, and an activation enthalpy ΔH_x. The experimental conditions enter the model in the form of the absolute temperature θ and the nominal strain rate $\dot{e}$, k_B is Boltzmann's constant, and R denotes the universal gas constant. A set of model parameters was calibrated from the uniaxial tensile tests and the resulting curves in Fig. 27 demonstrate that the Ree–Eyring theory is well capable of reproducing the rate and temperature dependence of the investigated PVDF grade. The parameters of the calibrated model are given in Table 2. Softening was not observed in the net axial stress *vs.* logarithmic strain response for tensile tests at quasi-static rate and room temperature. However, for elevated strain rates and ambient temperatures of −20 °C and 4 °C, a small amount of softening was observed upon yield. Strain softening at the onset of yielding is commonly attributed to either intrinsic softening such as ageing of the matrix material [41–43] or to softening caused by separation of the particles from the matrix at the interface [15]. However, since the particles appear to be undeformed upon failure (see Figs. 9 and 23), particle–matrix decohesion cannot be considered a source of softening in this material. However, gathering conclusive evidence on the origin of strain softening in this material is considered out of scope for this study.

For all tests, increasing strain hardening was observed for increasing deformation. However, the overall strain hardening decreased with an increasing ambient temperature or strain rate. Also, a transition from

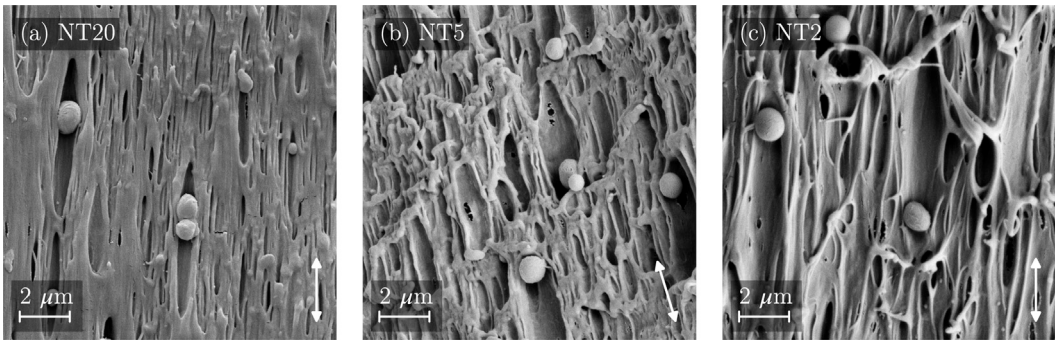

Fig. 23. Impact of the stress triaxiality ratio on the morphology in NT specimens (post failure) for different notch radii: (a) NT20, (b) NT5, (c) NT2. The white arrows indicate the tensile stress direction.

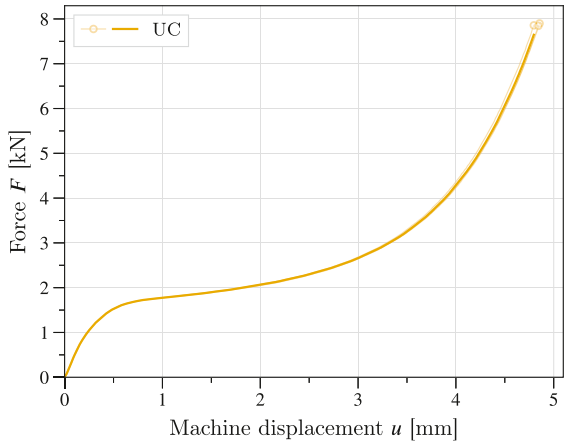

Fig. 24. Force *vs.* machine displacement response of the quasi-static UC tests at room temperature ($T = 25$ °C).

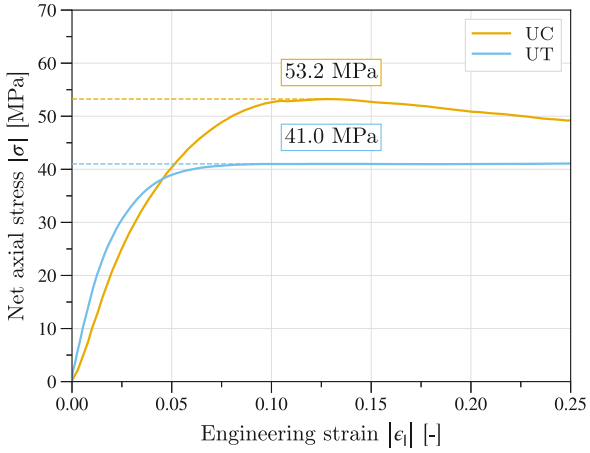

Fig. 25. Comparison of the net axial stress at the onset of yielding under tension and compression.

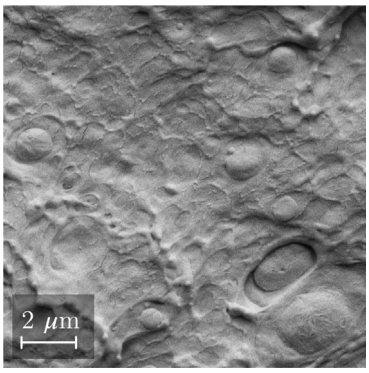

Fig. 26. SEM micrograph of the morphology in the centre of a UC specimen (post deformation).

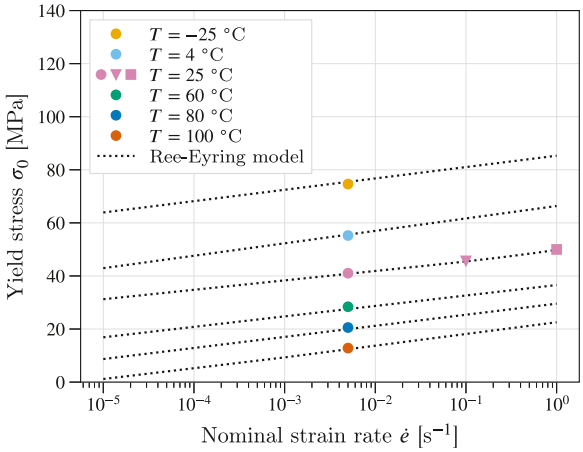

Fig. 27. Yield stress σ_0 *vs.* nominal strain rate $\dot{e}$ from uniaxial tensile tests at different strain rates and temperatures, complemented by a fitted Ree–Eyring model.

a gradually increasing strain hardening to a more abrupt increase in hardening at large strains was observed for a decrease in strain rate or increase in temperature. In polymers, such an abrupt increase in strain hardening at large strains is commonly attributed to reorientation as well as locking of the polymers molecular backbone and is therefore intrinsic to the matrix material [44]. In the present case, the transition from a gradually increasing hardening to an abrupt onset at large strains was likely caused by saturation of the longitudinal strain in the notch. The subsequent associated spread of the deformation to the neighbouring material outside the gauge section, featuring a larger cross section, has to be assumed the main driver of the stark increase in the reaction force and stress. Also, an increased stress triaxiality ratio and correspondingly increased void growth were found to reduce the rate of strain hardening at large strains, suggesting that void formation and growth had a pronounced influence on the hardening of the material at large strains. Similarly, when the strain rate $\dot{e}$ was elevated to $0.01\,s^{-1}$ and $1.0\,s^{-1}$, an increased volume strain was observed, corresponding to decreased strain hardening. Furthermore, a more gradually increasing hardening was observed in the case of the elevated strain rates, possibly caused by increased thermal softening due to limited heat diffusion.

The longitudinal stress at the onset of yielding was found to be approximately similar in all UT and NT experiments featuring different notch radii. Therefore, the material exhibited pressure-sensitive yielding. This behaviour is possibly caused by the presence of voids in the material [45,46]. Considering the SEM images of samples deformed at room temperature, the embedded PE particles did not appear to be deformed, suggesting that separation of the particles and surrounding matrix happened before yielding of the particles. However, this could not be confirmed from the volume strain measurements since the onset of void nucleation cannot be identified on the surface of a specimen as separation at the phase boundary does not necessarily cause an increase in overall volume strain. Furthermore, the accuracy of the DIC derived volume strain measurements is questionable at small deformations.

Two sources of void formation were observed in the SEM images: (i) separation at the phase boundary between particles and matrix and (ii) void nucleation in the matrix material. The relative contribution from the two sources could not be determined from the SEM images. Void nucleation by particle–matrix decohesion has been observed in other filled polymers, e.g. mineral filled PVC, causing void formation from the onset of yielding [14,15]. Cavitation within the matrix material itself is commonly observed in neat semi-crystalline polymers such as PA6, PA11 and HDPE. There, the voids form in the amorphous phase of the spherulitic microstructure and are constrained by the crystalline lamellae [17–19]. However, in this study, the SEM images neither allowed the microstructure of the material nor the origin of cavitation to be identified. It should here be noted that the specimens were imaged using SEM after being stored for several weeks. Hence, any phenomena influenced by stress relaxation could not be studied.

Stress triaxiality, ambient temperature, and strain rate all had a pronounced impact on the degree of void growth during deformation of the specimens. The interrelationship between an elevated stress triaxiality and an increased void growth conforms to previous studies on similar materials [16,29]. The increased dilation observed for the UT tests at elevated strain rates could be caused by the increased stress level, promoting separation of the particles from the matrix at the interface and void nucleation in the matrix material.

The volume strain and void growth were significantly reduced at an ambient temperature of 60 °C, and no void growth was observed at temperatures of 80 °C and 100 °C. Several other studies on PVDF also found a decrease of volume strain with an increasing temperature [12,16]. The stress level was also significantly reduced at higher temperatures, possibly reducing the material's tendency to nucleate voids. Also, the highly deformed neck region in the case of the 100 °C sample was translucent in appearance. Fig. 28 shows the microstructure of an undeformed material sample, heated to 100 °C and subsequently cryogenically cracked open, where this translucency was not observed. PVDF thin films featuring a thickness of less than 200 μm have been found to turn transparent upon large stretches at room temperature [1]. Investigating macroscopic specimens, André-Castagnet and Tencé-Girault [12] observed a tendency for PVDF to turn translucent when subjected to large deformations and elevated temperatures up to 150 °C. Thereby, lower strain rates and higher temperatures were found to promote translucency. That behaviour was attributed to a reduced tendency for voiding. Hence, in the sense that both mechanical stress and increased temperatures prevent voiding and therefore promote translucency, the results of this study are in line with other findings in the literature. The PE particles could not be identified in SEM micrographs of the samples which had been deformed at 100 °C, whereas the particles were still present in SEM micrographs of undeformed material that had been heated to the same temperature (Fig. 28). Hence, the combination of both mechanical stress and an elevated temperature must be responsible for the particles' disappearance. An explanation might be that the particles melt as a result of the temperature nearing their melting point in combination with pressure from the deforming surrounding matrix. Subsequently, elongation and shear forces acting on the particles in their molten state may lead to their dissolution.

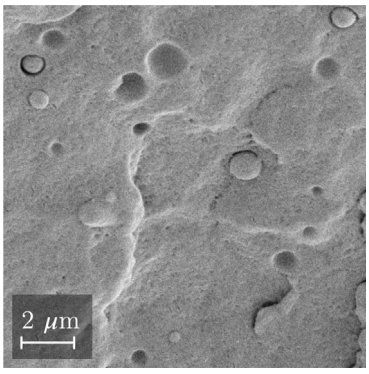

Fig. 28. SEM micrograph of an undeformed PVDF sample that has been heated to a temperature of 100 °C and subsequently cryogenically cracked open.

5. Conclusions

This study investigated the influence of temperature, strain rate and stress triaxiality on the large-strain response of a commercial PVDF copolymer. The following conclusion can be drawn:

- The material contained a low fraction of spherical PE particles with an average size in the order of 1 μm. The PE particles were found to promote void formation by separation at the interface between particles and matrix during deformation.
- The material exhibited a temperature-dependent and strain-rate-dependent behaviour, where the stress level increased for increasing strain rate and decreasing temperature.
- Pressure-sensitive yielding was observed in tensile tests featuring different stress triaxialities as well as compression tests.
- Pronounced plastic dilation was observed for all tensile tests. The plastic dilation increased with increasing deformation and was promoted through elevated stress triaxiality. On the microscale, the plastic dilation corresponded with void growth initiated by separation at the phase boundary as well as void nucleation in the matrix.
- No plastic dilation was observed for ambient temperatures of 80 °C and 100 °C. Accordingly, no voids were identified on the microscale.

CRediT authorship contribution statement

Jonas Hund: SEM imaging, Data curation, Visualisation, Writing – original draft. **Henrik Møgster Granum:** Experiment planning, Experiment execution, Data curation, Writing – review & editing. **Sindre Nordmark Olufsen:** Consultation, Writing – original draft. **Petter Henrik Holmström:** Consultation, Writing – review & editing. **Joakim Johnsen:** Experiment planning, Consultation, Writing – review & editing. **Arild Holm Clausen:** Supervision, Consultation, Writing – review & editing.

Declaration of competing interest

The authors declare the following financial interests/personal relationships which may be considered as potential competing interests: Jonas Hund reports financial support was provided by Research Council of Norway. Sindre Nordmark Olufsen reports financial support was provided by Equinor ASA. Henrik Mogster Granum reports financial support was provided by Enodo AS. Joakim Johnsen reports financial support was provided by Enodo AS. Jonas Hund reports financial support and equipment, drugs, or supplies were provided by Baker Hughes. Jonas Hund reports financial support was provided by Equinor ASA.

Data availability

The raw/processed data required to reproduce these findngs cannot be shared at this time due to technical or time limitations.

Acknowledgements

The authors wish to thank the Research Council of Norway for funding through the Petromaks 2 programme, Contract No. 317673. The financial support from Equinor, Norway, Baker Hughes, United Kingdom, and Enodo, Norway is also acknowledged. The authors also gratefully appreciate the financial support from the Research Council of Norway through the Centre for Advanced Structural Analysis, Project No. 237885 (SFI-CASA).

Appendix. Complementary plots to the UT strain rate tests

Figs. 29 and 30 show the force *vs.* displacement and force *vs.* log. longitudinal strain responses of the UT tests at different strain rates at room temperature, respectively. The elongation of the whole specimen in comparison to the elongation of the gauge section for the UT tests at the intermediate strain rate $\dot{e}$ of 0.1 s^{-1} is shown in Fig. 31. Fig. 29 shows that for large deformations the reaction force and overall specimen elongation, represented by the machine displacement u, were still increasing, while the material in the gauge section used for DIC did no longer experience any elongation (see Fig. 31). Therefore, Figs. 30 and 31 shall illustrate that the DIC-derived quantities (based on the elongation of the gauge section) such as the longitudinal strain ϵ_l could not reproduce the increasing overall deformation shown in Figs. 29 and 31 for longitudinal strain $\epsilon_l \geq 1.6$.

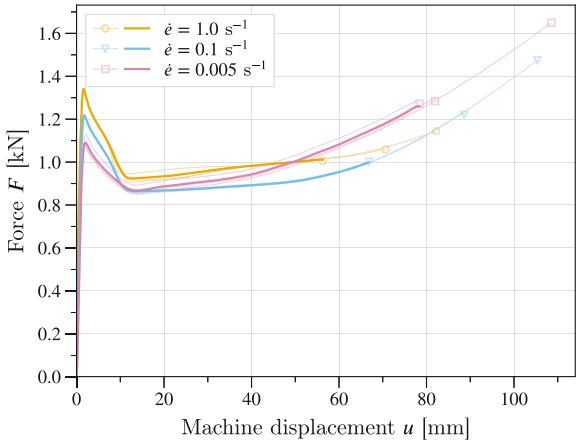

Fig. 29. Force *vs.* displacement response of UT tests at three strain rates and room temperature (T = 25 °C).

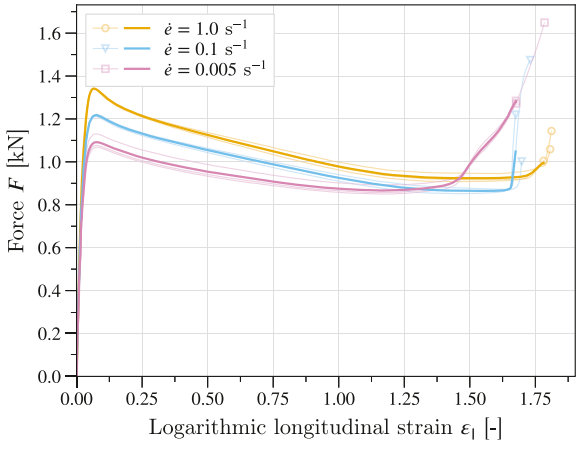

Fig. 30. Force *vs.* log. longitudinal strain response of UT tests at three strain rates and room temperature (T = 25 °C).

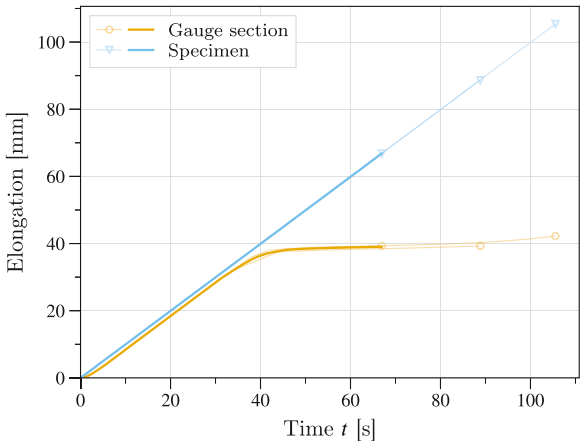

Fig. 31. Elongations of the whole specimen and the specimen gauge section for the UT tests at the intermediate strain rate $\dot{e}$ = 0.1 s^{-1}.

References

[1] N. Osaka, K. Yanagi, H. Saito, The optical transparency and structural change of quenched poly(vinylidene fluoride) caused by cold-drawing, Polym. J. 45 (10) (2013) 1033–1040, http://dx.doi.org/10.1038/pj.2013.26.

[2] D. Girard, S. Castagnet, J.L. Gacougnolle, G. Hoschstetter, On the relevance of a notch creep test for the comprehension and prediction of slow crack growth in PVDF, Polym. Test. 26 (7) (2007) 937–948, http://dx.doi.org/10.1016/j.polymertesting.2007.06.011.

[3] S. Castagnet, J.-L. Gacougnolle, P. Dang, Correlation between macroscopical viscoelastic behaviour and micromechanisms in strained α polyvinylidene fluoride (PVDF), Mater. Sci. Eng. A 276 (1) (2000) 152–159, http://dx.doi.org/10.1016/S0921-5093(99)00320-2.

[4] M.G. Broadhurst, G.T. Davis, Physical basis for piezoelectricity in PVDF, Ferroelectrics 60 (1) (1984) 3–13, http://dx.doi.org/10.1080/00150198408017504.

[5] A. Vinogradov, F. Holloway, Electro-mechanical properties of the piezoelectric polymer PVDF, Ferroelectrics 226 (1) (1999) 169–181, http://dx.doi.org/10.1080/00150199908230298.

[6] P. Ueberschlag, PVDF piezoelectric polymer, Sensor Review 21 (2) (2001) 118–126, http://dx.doi.org/10.1108/02602280110388315.

[7] W.M. Prest, D.J. Luca, The morphology and thermal response of high-temperature – crystallized poly(vinylidene fluoride), J. Appl. Phys. 46 (10) (1975) 4136–4143, http://dx.doi.org/10.1063/1.321438.

[8] A. Ambrosy, K. Holdik, Piezoelectric PVDF films as ultrasonic transducers, J. Phys. E: Sci. Instrum. 17 (10) (1984) 856–859, http://dx.doi.org/10.1088/0022-3735/17/10/011.

[9] X. Wang, C. Xiao, H. Liu, Q. Huang, H. Fu, Fabrication and properties of PVDF and PVDF-HFP microfiltration membranes, J. Appl. Polym. Sci. 135 (40) (2018) 46711, http://dx.doi.org/10.1002/app.46711.

[10] A.V. Shirinov, W.K. Schomburg, Pressure sensor from a PVDF film, Sensors Actuators A 142 (1) (2008) 48–55, http://dx.doi.org/10.1016/j.sna.2007.04.002.

[11] M. Challier, J. Besson, L. Laiarinandrasana, R. Piques, Damage and fracture of polyvinylidene fluoride (PVDF) at 20 °C: Experiments and modelling, Eng. Fract. Mech. 73 (1) (2006) 79–90, http://dx.doi.org/10.1016/j.engfracmech.2005.06.007.

[12] S. André-Castagnet, S. Tencé-Girault, Relationships between mechanical tensile behavior and micro-mechanisms in poly(vinylidene fluoride) at high temperatures: Influence of the molecular weight distribution, J. Macromol. Sci. B 41 (4–6) (2002) 957–976, http://dx.doi.org/10.1081/MB-120013076.

[13] M.D.C. Silva, D.A. Laurentino, M.F. da Costa, C.A. da Costa Neto, Whitening Generation in PVDF Under Cyclic Loading, in: ASME 2015 34th International Conference on Ocean, Offshore and Arctic Engineering, American Society of Mechanical Engineers Digital Collection, 2015, http://dx.doi.org/10.1115/OMAE2015-41303.

[14] S. Olufsen, A.H. Clausen, O.S. Hopperstad, Influence of stress triaxiality and strain rate on stress-strain behaviour and dilation of mineral-filled PVC, Polym. Test. 75 (2019) 350–357, http://dx.doi.org/10.1016/j.polymertesting.2019.02.018.

[15] A.S. Ognedal, A.H. Clausen, T. Berstad, T. Seelig, O.S. Hopperstad, Void nucleation and growth in mineral-filled PVC - An experimental and numerical study, Int. J. Solids Struct. 51 (7–8) (2014) 1494–1506, http://dx.doi.org/10.1016/j.ijsolstr.2013.12.042.

[16] S. Castagnet, S. Girault, J.L. Gacougnolle, P. Dang, Cavitation in strained polyvinylidene fluoride: mechanical and X-ray experimental studies, Polymer 41 (20) (2000) 7523–7530, http://dx.doi.org/10.1016/S0032-3861(00)00077-X.

[17] A. Pawlak, A. Galeski, A. Rozanski, Cavitation during deformation of semicrystalline polymers, Prog. Polym. Sci. 39 (5) (2013) 921–958, http://dx.doi.org/10.1016/j.progpolymsci.2013.10.007.

[18] C. Ovalle, P. Cloetens, H. Proudhon, T.F. Morgeneyer, L. Laiarinandrasana, Nanocavitation mechanisms in deformed High Density PolyEthylene (HDPE) using synchrotron radiation NanoTomography, Polymer 229 (June) (2021) 123959, http://dx.doi.org/10.1016/j.polymer.2021.123959.

[19] L. Laiarinandrasana, O. Klinkova, F. Nguyen, H. Proudhon, T.F. Morgeneyer, W. Ludwig, Three dimensional quantification of anisotropic void evolution in deformed semi-crystalline polyamide 6, Int. J. Plast. 83 (2016) 19–36, http://dx.doi.org/10.1016/j.ijplas.2016.04.001.

[20] R. Greco, M.F. Astarita, L. Dong, A. Sorrentino, Polycarbonate/ABS blends: Processability, thermal properties, and mechanical and impact behavior, Adv. Polym. Technol. 13 (4) (1994) 259–274, http://dx.doi.org/10.1002/adv.1994.060130402.

[21] T. Seelig, E. Van der Giessen, A cell model study of crazing and matrix plasticity in rubber-toughened glassy polymers, Comput. Mater. Sci. 45 (3) (2009) 725–728, http://dx.doi.org/10.1016/j.commatsci.2008.05.024.

[22] E. Van der Giessen, T. Seelig, Computational modeling of rubber-toughening in amorphous thermoplastic polymers: a review, Int. J. Fract. 196 (1) (2015) 207–222, http://dx.doi.org/10.1007/s10704-015-0066-6.

[23] S.Y. Fu, X.Q. Feng, B. Lauke, Y.W. Mai, Effects of particle size, particle/matrix interface adhesion and particle loading on mechanical properties of particulate-polymer composites, Composites B 39 (6) (2008) 933–961, http://dx.doi.org/10.1016/j.compositesb.2008.01.002.

[24] P.-Y.B. Jar, R. Lee, T. Shinmura, K. Konishi, Rubber particle cavitation on toughness enhancement of SMI-modified poly(acrylonitrile-butadiene-styrene), J. Polym. Sci. B: Polym. Phys. 37 (14) (1999) 1739–1748, http://dx.doi.org/10.1002/(SICI)1099-0488(19990715)37:14<1739::AID-POLB16>3.0.CO;2-Z.

[25] J.P.F. Inberg, R.J. Gaymans, Co-continuous polycarbonate/ABS blends, Polymer 43 (8) (2002) 2425–2434, http://dx.doi.org/10.1016/S0032-3861(01)00813-8.

[26] A.S. Ognedal, A.H. Clausen, A. Dahlen, O.S. Hopperstad, Behavior of PVC and HDPE under highly triaxial stress states: An experimental and numerical study, Mech. Mater. 72 (2014) 94–108, http://dx.doi.org/10.1016/j.mechmat.2014.02.002.

[27] G. Boisot, L. Laiarinandrasana, J. Besson, C. Fond, G. Hochstetter, Experimental investigations and modeling of volume change induced by void growth in polyamide 11, Int. J. Solids Struct. 48 (19) (2011) 2642–2654, http://dx.doi.org/10.1016/j.ijsolstr.2011.05.016.

[28] S. Castagnet, Y. Deburck, Relative influence of microstructure and macroscopic triaxiality on cavitation damage in a semi-crystalline polymer, Mater. Sci. Eng. A 448 (1) (2007) 56–66, http://dx.doi.org/10.1016/j.msea.2006.11.100.

[29] N. Brusselle-Dupend, E. Rosenberg, J. Adrien, Characterization of cavitation development while tensile testing PVF2 using 3D X-ray microtomography, Mater. Sci. Eng. A 530 (2011) 36–50, http://dx.doi.org/10.1016/j.msea.2011.09.009.

[30] A. Pawlak, A. Galeski, Plastic Deformation of Crystalline Polymers: The Role of Cavitation and Crystal Plasticity, Macromolecules 38 (23) (2005) 9688–9697, http://dx.doi.org/10.1021/ma050842o.

[31] S. Humbert, O. Lame, J.M. Chenal, C. Rochas, G. Vigier, New Insight on Initiation of Cavitation in Semicrystalline Polymers: In-Situ SAXS Measurements, Macromolecules 43 (17) (2010) 7212–7221, http://dx.doi.org/10.1021/ma101042d.

[32] S.N. Olufsen, A.H. Clausen, D.W. Breiby, O.S. Hopperstad, X-ray computed tomography investigation of dilation of mineral-filled PVC under monotonic loading, Mech. Mater. 142 (July 2019) (2020) 103296, http://dx.doi.org/10.1016/j.mechmat.2019.103296.

[33] M. Andersen, O.S. Hopperstad, A.H. Clausen, Volumetric strain measurement of polymeric materials subjected to uniaxial tension, Strain 55 (4) (2019) http://dx.doi.org/10.1111/str.12314.

[34] J. Johnsen, F. Grytten, O.S. Hopperstad, A.H. Clausen, Influence of strain rate and temperature on the mechanical behaviour of rubber-modified polypropylene and cross-linked polyethylene, Mech. Mater. 114 (2017) 40–56, http://dx.doi.org/10.1016/j.mechmat.2017.07.003.

[35] J. Johnsen, F. Grytten, O.S. Hopperstad, A.H. Clausen, Experimental set-up for determination of the large-strain tensile behaviour of polymers at low temperatures, Polym. Test. 53 (2016) 305–313, http://dx.doi.org/10.1016/j.polymertesting.2016.06.011.

[36] G.A. Holzapfel, in: Repr (Ed.), Nonlinear Solid Mechanics, Wiley, Chichester, 2010, XIV, 455 S..

[37] Y.S. Urzhumtsev, Time-temperature superposition. Review, Polym. Mech. 11 (1) (1975) 57–72, http://dx.doi.org/10.1007/BF00855426.

[38] C. Bauwens-Crowet, J.C. Bauwens, G. Homès, Tensile yield-stress behavior of glassy polymers, J. Polym. Sci. A-2: Polym. Phys. 7 (4) (1969) 735–742, http://dx.doi.org/10.1002/pol.1969.160070411.

[39] A.V. Tobolsky, R.D. Andrews, Systems Manifesting Superposed Elastic and Viscous Behavior, J. Chem. Phys. 13 (1) (1945) 3–27, http://dx.doi.org/10.1063/1.1723966.

[40] T. Ree, H. Eyring, Theory of Non-Newtonian Flow. I. Solid Plastic System, J. Appl. Phys. 26 (7) (1955) 793–800, http://dx.doi.org/10.1063/1.1722098.

[41] H.E. Meijer, L.E. Govaert, Mechanical performance of polymer systems: The relation between structure and properties, Prog. Polym. Sci. (Oxford) 30 (8–9) (2005) 915–938, http://dx.doi.org/10.1016/j.progpolymsci.2005.06.009.

[42] L.C.A. van Breemen, T.A.P. Engels, E.T.J. Klompen, D.J.A. Senden, L.E. Govaert, Rate- and temperature-dependent strain softening in solid polymers, J. Polym. Sci. B: Polym. Phys. 50 (24) (2012) 1757–1771, http://dx.doi.org/10.1002/polb.23199.

[43] L.E. Govaert, P.H.M. Timmermans, W.A.M. Brekelmans, The Influence of Intrinsic Strain Softening on Strain Localization in Polycarbonate: Modeling and Experimental Validation, J. Eng. Mater. Technol. 122 (2) (1999) 177–185, http://dx.doi.org/10.1115/1.482784.

[44] Z. Bartczak, A. Galeski, Plasticity Of Semicrystalline Polymers, Macromol. Symp. 294 (1) (2010) 67–90, http://dx.doi.org/10.1002/masy.201050807, URL: http://doi.wiley.com/10.1002/masy.201050807.

[45] A.C. Steenbrink, E. van der Giessen, On cavitation, post-cavitation and yield in amorphous polymer–rubber blends, J. Mech. Phys. Solids 47 (4) (1999) 843–876, http://dx.doi.org/10.1016/S0022-5096(98)00075-1.

[46] A. Needleman, A Continuum Model for Void Nucleation by Inclusion Debonding, J. Appl. Mech. 54 (3) (1987) 525–531, http://dx.doi.org/10.1115/1.3173064.